optica

Optical matter machines: angular momentum conversion by collective modes in optically bound nanoparticle arrays

John Parker,[1,3] Curtis W. Peterson,[2,3] Yuval Yifat,[3] Stuart A. Rice,[2,3] Zijie Yan,[4] Stephen K. Gray,[5] and Norbert F. Scherer[2,3,*]

[1]*Department of Physics, The University of Chicago, Chicago, Illinois 60637, USA*
[2]*Department of Chemistry, The University of Chicago, Chicago, Illinois 60637, USA*
[3]*James Franck Institute, The University of Chicago, Chicago, Illinois 60637, USA*
[4]*Department of Applied Physical Sciences, University of North Carolina at Chapel Hill, Chapel Hill, North Carolina 27599, USA*
[5]*Center for Nanoscale Materials, Argonne National Laboratory, Lemont, Illinois 60439, USA*
Corresponding author: nfschere@uchicago.edu

The creation of optically powered self-assembling nano-to-meso-scale machines that do work is a long-standing goal in photonics. We demonstrate an optical matter (OM) machine that converts the spin angular momentum (SAM) of light into orbital angular momentum (OAM) to do mechanical work. The specific OM machine we study is based on a sixfold symmetric hexagonally ordered nanoparticle array that operates as an OM "gear" that is assembled and made to rotate in a circularly polarized Gaussian beam. The rotational symmetry of the OM gear leads to a selection rule for the allowed scattering modes based on their angular momentum. Electrodynamics calculations show that the collective scattering modes with the largest angular momentum scatter strongly in the transverse direction. Simulations and experiments show that the angular momentum that accompanies the scattered light causes a "negative torque" response on the OM gear and drives a "probe" particle placed outside the OM gear around the gear in an asymmetric force field analogously to Brownian ratchets. The gear–probe OM machine concept can be expanded to applications in nanofluidics and particle sorting.   © 2020 Optical Society of America under the terms of the OSA Open Access Publishing Agreement

https://doi.org/10.1364/OPTICA.396147

1. INTRODUCTION

Particles in an optical field are subject to electrodynamic forces that can be used to manipulate them with great control and precision. The most common application of this principle is optical trapping [1,2]. When multiple particles are present in an optical trap, they electrodynamically interact with each other via their mutually scattered light. This interaction can be strong enough to create interparticle forces that lead to ordered arrays known as optical matter (OM), even in the presence of random Brownian forces in solution [3–9]. OM arrays are non-equilibrium systems due to a continuous flux of optical (beam) power through the material. Recent work has shown that the dynamic behavior of OM arrays is related to their shape and symmetry [10–18]. Light scattering from nanoparticle (NP) arrays can bring about unusual phenomena such as apparent "non-reciprocal" forces [14,18], negative torque [19–21], and non-conservative forces [22]. While there has been steady progress toward understanding how tailoring incident fields can affect the dynamics and structure of OM arrays [23–25], less attention has been given to the characteristics of the light scattered by the arrays (for a review of light scattering by arrays of particles and holes; see [26]).

Previous work has introduced the idea of driving and controlling the spinning of individual NPs using the spin angular momentum (SAM) of light in circularly polarized optical tweezers, referred to as "optical torque wrenches" [27–31]. This has been extended to arrays of NPs, where an optical torque wrench can generate orbital rotation through their interparticle interactions [19,20,32]. Moreover, optical traps have also made possible the design of single particle micrometer and nanometer size heat engines capable of converting heat into work [33–35]. Therefore, optically assembled and rotationally driven OM arrays might be the basis for nano-scale machines capable of doing work. The possibility of using light–matter interactions to convert SAM into orbital angular momentum (OAM) has been demonstrated and can be used as the driving mechanism of such machines [36].

In this paper, we demonstrate that the orbital motion of OM arrays is caused and controlled by a set of collective scattering modes that carry OAM away from the OM array. Collective modes with the largest OAM content are found to have strong angular scattering in the transverse direction. We utilize these collective scattering modes of the OM array as an SAM–OAM converter, which we call an OM "gear," and show that an additional particle,

referred to as the probe particle, placed in proximity to this OM gear will couple to the collective modes via scattered fields and orbit in the opposite direction of the OM gear's rotation.

A mechanical analog of the SAM–OAM converter is a planetary gear machine [37]—schematically shown in Fig. 1(a). Work is performed in the gear system by rotating a crank connected to a large gear. Both the shaft and gear are shown exhibiting right-handed rotation (denoted by red arrows; the convention of pointing one's thumb toward the source is used). A second, smaller gear is coupled to the larger gear, causing it to rotate and orbit the large gear. The small gear rotates with an opposite left-handed rotation (denoted by the green arrow). A fixed ring gear provides radial confinement and causes the small gear to perform a right-handed orbit around the large gear.

The analogous OM machine is depicted in Fig. 1(b). The crank is replaced with a right-hand circularly (RHC) polarized optical beam. The material constituents of the OM gear, Ag NPs of radius $R_p = 75$ nm, are attracted to the high intensity region of the focused beam. Multiple particles trapped in the beam self-organize into a hexagonal lattice geometry due to rotationally symmetric optical binding interactions when the incident light is circularly polarized [20]. With an incident wavelength of $\lambda = 800$ nm ($\lambda_w = \lambda/n_w \approx 600$ nm in water, where $n_w = 1.33$), the optical binding distance is $\delta = \lambda_w \approx 600$ nm. An assembled 7NP OM array operates as an OM gear; the angular momentum of the scattered field provides the torque for the gear to rotate. For the NP properties and geometry considered here, the OM gear exhibits a *negative torque*, i.e., it rotates in the left-handed direction despite the right-handed spin of the incident photons [20].

Surprisingly, when a probe particle (Ag NP with radius $R_p = 100$ nm) is placed outside the OM gear, it orbits in the right-handed direction, analogous to the orbital motion of the small gear in the planetary gear mechanical machine (Fig. 1). This observed counter-rotation can be understood as a demonstration of conservation of angular momentum: if the OM gear is rotating with handedness that is opposite to that of the incident light, it must be that a net positive quantity of angular momentum is scattered by the OM gear. The probe particle feels this outgoing positive angular momentum and is driven to orbit around the

OM gear [Fig. 1(c)]. Radial confinement of the probe is provided by an inward phase gradient of the converging beam optical trap (see Supplement 1), analogous to the use of a fixed ring gear that radially confines the small gear in the mechanical machine.

2. OM GEAR IS AN ANGULAR MOMENTUM CONVERTER

Since the total angular momentum of the system (electromagnetic field and NPs) is conserved, a negative torque on the gear necessitates increased angular momentum in the emanating field. Scattered light from the OM gear can be decomposed into collective multipolar modes, labeled $e_{n,m}$ and $m_{n,m}$ for electric and magnetic modes, respectively; n is the order, and m is the azimuthal index of the mode. These modes are eigenfunctions of the angular momentum operator, with eigenvalue m; this description is analogous to that of quantum mechanical angular momentum states where the spherical harmonics are eigenfunctions of the angular momentum operator [38]. Each collective mode continuously carries angular momentum, L_z^{mn}, away from the OM gear at a rate

$$\frac{d}{dt}L_z^{mn} = \frac{m}{2k}\left(\varepsilon_b C_{e,scat}^{mn} + \mu_b C_{m,scat}^{mn}\right) \qquad m \neq m_{inc}, \quad (1)$$

where $C_{e,scat}^{mn}$ and $C_{m,scat}^{mn}$ are the scattering cross sections of the electric and magnetic modes, respectively, and ε_b and μ_b are the permittivity and permeability of the medium, respectively (see Supplement 1 for details). In response, the OM gear feels a net recoil torque (spin and orbit) due to conservation of angular momentum.

Selection rules that restrict the allowed values of m based on conservation of angular momentum have been reported for rotationally symmetric NP arrays [19,39]. For an array with m_s-fold symmetry and incident light with m_{inc}, the allowed values of m are

$$m = m_{inc} + m_s q, \quad (2)$$

where q is a positive or negative integer. This selection rule forms the basis of our OM SAM–OAM machine: photons with $m_{inc} = +1$ incident on the $m_s = 6$-fold symmetric OM gear are
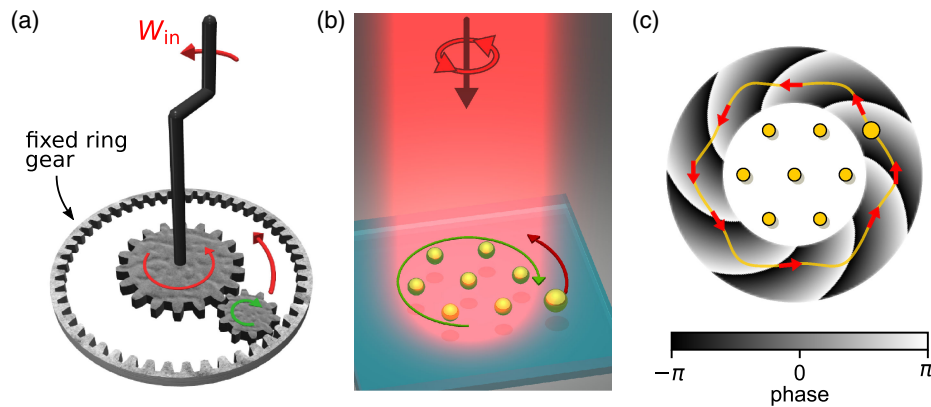

Fig. 1. Designing an optical matter machine. (a) A planetary mechanical gear machine consisting of a large gear made to rotate by a crank and a small gear that is driven to rotate and orbit. A fixed ring gear provides radial confinement and causes the small gear to orbit the large gear. The gears couple such that the small gear rotates with the opposite handedness and orbits with the same handedness as the large gear's rotation. (b) An analogous optical matter machine. The 7NP array acts as a large OM gear that converts spin angular momentum into orbital angular momentum that is imparted on a smaller OM gear (the probe particle), driving its orbital motion. (c) The phase profile of the $e_{7,7}$ mode in the transverse plane outside the OM gear. The phase profile, $\psi \propto \exp(i7\phi)$, provides a circulation of momentum around the OM gear, with $m = 1 + 6$ phase wrappings. A path for the probe particle's orbital motion is shown in yellow.

converted into collective scattering modes with $m = -5, +1, +7$. Larger m values can be neglected due to the size of the OM gear as determined by Wiscombe's criterion [40].

The magnitude and directionality of light scattered by the $m = -5$ and $m = +7$ modes determine the field that the probe particle experiences. The calculated phase profile of the $e_{7,7}$ mode scattered in the transverse plane of the OM gear is depicted in Fig. 1(c). The yellow curve is the preferred path of the probe particle to move around the OM gear. We will demonstrate that the $e_{7,7}$ mode is the dominant contribution to the transversely scattered OAM, and is therefore responsible for the right-handed driven orbital motion of the probe particle.

3. COLLECTIVE SCATTERING MODES OF THE OM GEAR

The relationship between angular momentum and scattering cross sections in Eq. (1) motivates examination of the mode-dependent spectroscopic properties of the OM gear. The collective scattering modes in the OM gear emerge in the wavelength-dependent scattering cross section of the OM gear as it is built particle-by-particle in an optical trap. The scattering cross sections shown in Fig. 2(a) demonstrate that the single particle Mie resonance ($\lambda = 600$ nm) is converted into a new resonance ($\lambda = 740$ nm) as particles are added to the array. We refer to this emergent peak as a *collective scattering resonance* (CSR) of the OM array. Electric field intensity plots of the single particle Mie resonance and the CSR are shown as insets to Fig. 2(a).

In the limit of a large lattice, the CSR becomes spectrally more narrow and approaches the well-known surface lattice resonance (SLR) of an infinitely extended array [26,41]. Figure S2

in Supplement 1 shows the results of simulations of hexagonally ordered 1–19 particle arrays and compares their scattering spectra to that of 331 particles to demonstrate this convergence.

We perform a multipole expansion of the scattered fields to obtain the mode-dependent composition of the CSR and their contributions to the far-field angular scattering (see Supplement 1). In our notation, if the azimuthal index m is omitted, a sum over m is applied while keeping n fixed, i.e., $e_n = \sum_m e_{nm}$ and $m_n = \sum_m m_{nm}$. Figure 2(b) shows the contribution of the e_n and m_n modes to the total scattering intensity up to $n = 7$ for the OM gear. Thus, the CSR is a superposition of many orthogonal modes; the e_1, e_5, e_7, and m_4 modes are most significant. The azimuthal index m obeys the rotational symmetry selection rule [Eq. (2)] with $m_s = 6$ symmetry. Therefore, the e_7 mode consists of three terms ($m = -5, 1, 7$), the e_5 mode consists of two terms ($m = 1, -5$), and the e_1 and m_4 modes consist of only one term ($m = 1$).

The far-field angular scattering of the OM gear shown in Fig. 2(c) exhibits strong, narrow lobes along the forward and backward directions and six transverse lobes lying in the x-y plane. Far-field angular scattering of the $e_{7,7}$ and $e_{5,-5}$ modes shown in Figs. 2(d) and 2(e) exhibits in-plane scattering with m phase wrappings. By contrast, the $m_{6,-5}$ mode in Fig. 2(f) exhibits out-of-plane angular scattering. Consequently, the $e_{7,7}$ and $e_{7,-5}$ modes couple strongly with positive and negative signs, respectively, to a probe particle located in the transverse plane while the $m_{6,-5}$ mode couples weakly. The $e_{7,7}$ mode is of particular interest due to its large angular momentum content and extremely flat angular profile. Visualizations of the remaining electric modes are shown in Fig. S3 in Supplement 1.
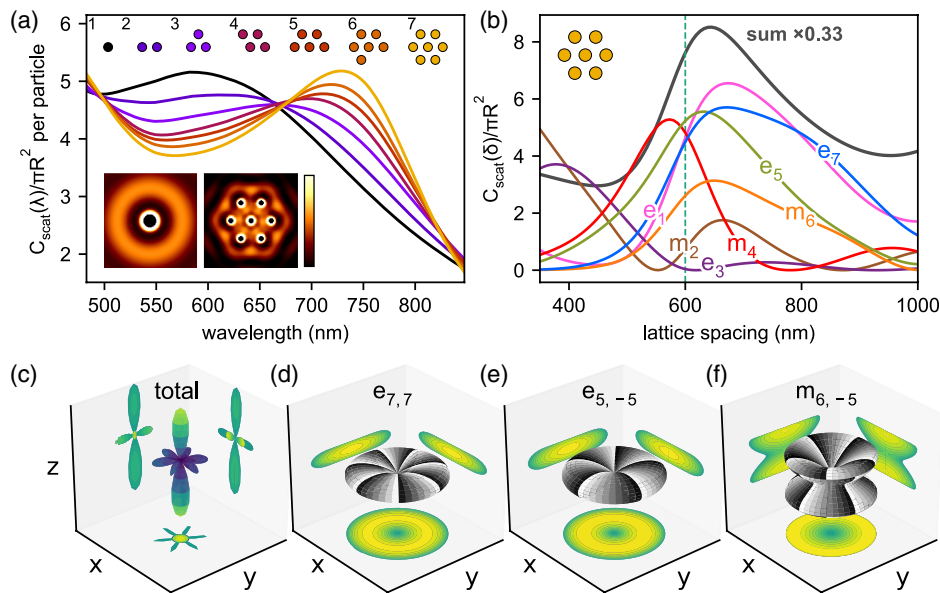

Fig. 2. Building an OM gear using optical binding forces and collective modes. (a) Per particle scattering cross section (normalized by πR_p^2, where $R_p = 75$ nm is the radius of a single NP) as the OM gear is built particle by particle with lattice spacing $\delta = 600$ nm in water ($n_b = 1.33$). A single particle Mie resonance ($\lambda = 600$ nm) is converted into a collective scattering resonance (CSR; $\lambda = 740$ nm). Insets show the field intensity of the single particle Mie resonance (left inset) and the CSR (right inset) at their respective resonant wavelengths. (b) Normalized scattering cross sections of the non-vanishing multipole modes of the OM gear as a function of lattice spacing, δ, at $\lambda = 800$ nm (optical binding distance shown as vertical dashed line). (c) Total far-field angular scattering intensity from the OM gear and projections onto the Cartesian planes. (d)–(f) Far-field angular scattering and phase profiles of the $e_{7,7}$, $e_{5,-5}$, and $m_{6,-5}$ modes, respectively.

4. SCATTERING OF ORBITAL ANGULAR MOMENTUM

As defined in Eq. (1), the azimuthal index m defines the rate of OAM scattered by the OM gear; modes with larger m have larger quantities of OAM. Figure 3(a) shows the mode-dependent contributions to the net angular momentum of the scattered light. The e_7 mode is strongest (and positive) due to the $m = 7$ term, while the e_5 and m_6 modes contribute negative angular momentum due to the $m = -5$ terms. The net angular momentum can be positive or negative depending on the lattice spacing, which results in a negative or positive recoil torque, respectively, on the OM gear. At the optical binding distance ($\delta = 600$ nm), the outgoing angular momentum is overall positive, resulting in a negative recoil torque on the OM gear.

We obtain a qualitative picture of the angular momentum around the OM gear by calculating the transverse Poynting vector, $\boldsymbol{S}_\parallel = (\boldsymbol{E} \times \boldsymbol{H})_\parallel$, in the xy plane. Streamlines of $\boldsymbol{S}_\parallel$ are shown in Fig. 3(b); the color-scale informs on the magnitude of $\boldsymbol{S}_\parallel$ relative to S_z of the incident field.

Inside the OM gear, $\boldsymbol{S}_\parallel$ spirals inward around each particle with the same handedness as the incident light. Outside the OM gear, there is a counterclockwise flow that the streamlines converge to. These streamlines suggest that if a probe particle is placed outside the OM gear it will feel a flow of electromagnetic energy and be driven to move along streamlines. The counterclockwise flow primarily comes from the $e_{7,7}$ mode that has a positive OAM directed in the xy plane.

The electrodynamic force on the probe can be calculated at positions outside the OM gear using the Maxwell stress tensor. The force can be separated into radial and azimuthal components, $\boldsymbol{F}(\boldsymbol{r}) = F_\rho(\boldsymbol{r})\hat{\boldsymbol{\rho}} + F_\phi(\boldsymbol{r})\hat{\boldsymbol{\phi}}$, that are shown in Figs. 3(c) and 3(d), respectively. The probe particle will generally move in 2D in response to the electrodynamic forces, and the radial force provides confinement that restricts the motion of the probe to a smaller domain. We define the stable 1D path for orbital motion of the probe particle such that the radial force vanishes and begets stability, i.e., $F_\rho = 0$ and $\partial F_\rho / \partial \rho < 0$. This path is shown as the dashed line in Figs. 3(c) and 3(d) and has a hexagonal-like shape.
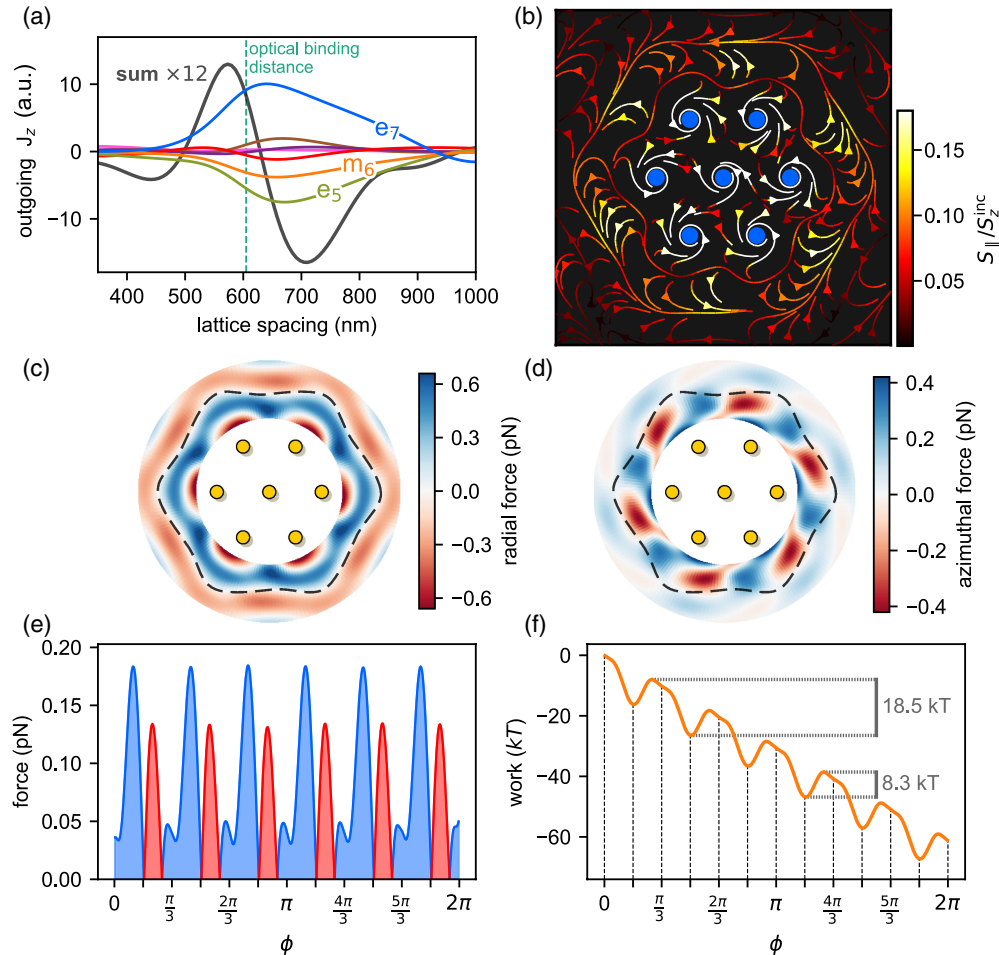

Fig. 3. Orbital angular momentum scattered by the OM gear can be used to do work. (a) Angular momentum carried away by the collective modes of the OM gear at $\lambda = 800$ nm. The net angular momentum is the sum of all such contributions, and can be positive or negative. The net outgoing angular momentum is positive at the optical binding distance ($\delta = 600$ nm). (b) Streamlines of the transverse Poynting vector in and around the OM gear. (c) Radial force map of the probe particle in an annular region outside the OM gear. The dashed line is a stable path where $F_\rho = 0$ and $\partial F_\rho / \partial \rho < 0$, where ρ is the particle's radial coordinate. (d) Azimuthal force map of the probe particle. The lattice spacing is $\delta = 600$ nm. (e) Component of the force tangential to the stable path, F_t. Blue regions are positive (counterclockwise), and red regions are negative (clockwise) force. (f) Work done on the probe particle as it moves along the stable path, $W = -\int F_t dl$ in units of $k_B T$, where k_B is Boltzmann's constant and $T = 298$ K.

The probe is not restricted to the stable path, but on average moves along it.

The azimuthal force can be positive (counterclockwise) or negative (clockwise) along the stable path. Stable positions along the path occur where the azimuthal force vanishes and begets stability along the path, i.e., $F_\phi = 0$ and $\partial F_\phi / \partial \phi < 0$. If the probe particle has enough thermal energy, it can hop from one stable position to another in either the clockwise or counterclockwise direction. However, since the positive forces generally outweigh the negative forces along the path, the probe particle prefers hopping in the counterclockwise direction due to the positive OAM from the $e_{7,7}$ mode as demonstrated by the projection of the azimuthal force along the stable path shown in Fig. 3(e). The work required to move the probe particle in the counterclockwise direction along the path, $W(\phi)$, is then an integral of this force curve, as shown in Fig. 3(f). $W(\phi)$ is periodic and tilted; the electrodynamic barrier for clockwise hops is about twice as large as that of counterclockwise hops. This type of work curve is analogous to 1D transport caused by Brownian fluctuations in asymmetric periodic potentials seen in forced thermal ratchets [42,43]. Although the work barriers are quite large for the probe to hop ($8.3\,k_BT$), this calculation assumes the seven particles in the gear remain stationary. The actual work required could be much lower when all particles are allowed to fluctuate due to higher dimensional pathways for the intruder to hop.

While the gear has a perfect sixfold symmetry, the presence of the probe particle breaks this symmetry and enables the combined machine to access azimuthal modes that violate the angular momentum selection rule, Eq. (2). In Fig. S10 in Supplement 1, we show that the effect of the probe on the gear causes it to scatter angular momentum into other azimuthal channels. However, the quantity of angular momentum is 50 times smaller than that carried by the $e_{7,7}$ mode, and the probe can be considered a perturbation to the scattered angular momentum selection rules.

Note that the OM gear does not need to be a sixfold symmetric hexagonal shape for the conversion of SAM to OAM to occur. Experimentally, the OM gear may contain additional particles or thermally fluctuate to different configurations. In such cases, the quantity of outgoing angular momentum in each of the modes [Fig. 3(a)] will be different.

5. DIRECTED TRANSPORT OF THE PROBE PARTICLE AROUND THE OM GEAR

A schematic of the thermal hopping of the probe around the OM gear along the stable path is shown in Fig. 4(a). The probe particle hops between six stable positions (denoted by solid orange squares) with a counterclockwise bias. In addition to the thermal hopping of the probe particle, the OM gear experiences a net recoil torque due to angular momentum being carried by light scattered from the CSR modes. Figure 2(b) shows that the recoil torque is negative at the given lattice spacing of the OM gear ($\delta = 600$ nm) since the e_7 mode carries more positive angular momentum than the total negative angular momentum of the e_5 and m_6 modes. This leads to a clockwise rotation of the OM gear—in the opposite direction of the probe particle's orbital motion, resulting in the counter-rotation of the OM machine.

A defocused but converging Gaussian beam is used in the simulations to provide an inward phase gradient to enhance the stability of the OM machine. Figure S5 in Supplement 1 shows that, without the inward radial phase gradient associated with the converging beam, the probe particle will escape the trap.

The probe particle must also be dissimilar in size from those NPs constituting the OM gear to prevent particle exchanges and rearrangement of the gear. Intuition suggests that a smaller probe particle may be preferred since it will scatter less light and cause less deformation in the OM gear, as shown in Fig. S6 in Supplement 1. However, a smaller probe will force its way into the
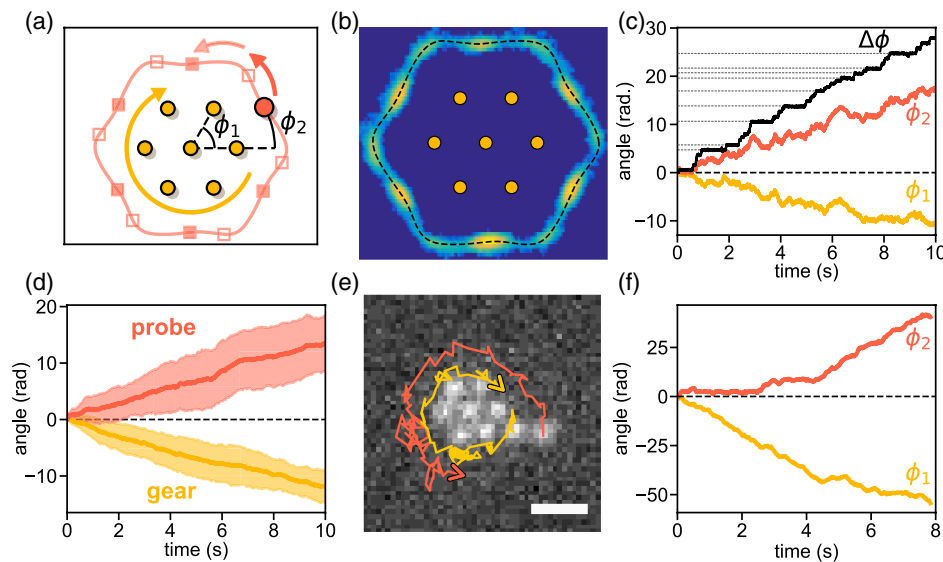

Fig. 4. Realizing an optical matter machine. (a) Schematic of the OM machine. Arrows denote the direction of preferred angular rotation. Filled and unfilled squares denote stable and unstable probe positions, respectively. The lattice spacing is $\delta = 600$ nm. (b) Probability density function of the probe's position relative to the OM gear from a 10 s Brownian dynamics simulation. (c) Time trajectories of the angular positions of the OM gear and probe particle. The difference angle, $\Delta\phi(t) = \phi_2(t) - \phi_1(t)$, is a monotonically increasing stepped function corresponding to angular jumps of the probe particle between stable positions. (d) Ensemble averaged angles of the probe and gear from 20 simulations. The shaded regions enclose the standard deviation of the angles at time t. (e) An image from a video of an experiment of an 8NP OM gear with a larger probe particle on its periphery. A 0.4 s trajectory of the OM gear and probe are superimposed. Scale bar, 1 μm. (f) Experimentally observed counter-rotation of the OM machine.

gear and break its structure, as shown in Fig. S7 in Supplement 1. Therefore, the probe particle must be larger than the NPs constituting the OM gear due to "non-reciprocal forces" that arise in NP hetero-dimers [18].

Given that the probe particle can be trapped in a local minimum of the work in Fig. 3(f), the driven transport of the probe particle will only occur in simulations with thermal energy and fluctuations. The counter-rotation of the OM machine was captured in a ($T = 298$ K) Brownian dynamics simulation that quantified the angular dynamics $\phi_1(t)$ of the OM gear and $\phi_2(t)$ of the probe particle as a function of time t. The path of the probe relative to the gear can be obtained by moving into a rotating reference frame such that the gear remains stationary and the probe orbits. A probability density function of the probe particle's position shown in Fig. 4(b) reveals the rounded hexagonal path of the probe and the six stable positions. The dashed line shows the stable path determined numerically in Fig. 3 and demonstrates agreement with the probability density from the probe particle trajectories.

The angular trajectories $\phi_1(t)$ and $\phi_2(t)$ for a single 10 s simulation shown in Fig. 4(c) confirm the counter-rotation of the gear and probe. With the starting condition $\phi_1 = \phi_2 = 0$ at $t = 0$ and defining the relative change in angle $\Delta\phi(t) = \phi_2(t) - \phi_1(t)$, we find that $\Delta\phi(t)$ strictly increases in time. The counter-rotation is shown to be statistically significant over an ensemble of 20 simulations for the same simulation conditions. Figure 4(d) shows the average and standard deviation of the ensemble of angular trajectories. Simulations with hydrodynamic interactions were also performed (see Fig. S8 in Supplement 1). Hydrodynamic rotation-translation (RT) coupling causes the OM gear to rotate with a smaller positive angular velocity, while the counterclockwise hopping of the probe is essentially unaffected.

6. EXPERIMENTAL CONFIRMATION OF THE OM MACHINE CONCEPT

We experimentally confirmed the predicted counter-rotation of the OM machine where the OM gear consists of eight equal-sized NPs (150 nm diameter Ag) with a larger probe particle (180–200 nm diameter Ag). Figure 4(e) shows an image from an experiment with an 8NP OM gear (hexagonal array plus one) and of a probe particle on its periphery. Trajectories for the probe (orange) and the eighth particle in the gear (yellow) of length 0.4 s starting from the frame are superimposed on the image. Figure 4(f) shows the trajectories of the angular positions $\phi_1(t)$ and $\phi_2(t)$ and confirms the counter-rotation over a longer time. Figure S9 in Supplement 1 shows an example of the counter-rotation for a 7NP OM gear, but it was not as persistent. Nevertheless, the experimentally observed counter-rotation for an 8NP OM machine suggests that these OM machines can be realized for a broader range of array geometries.

7. CONCLUSION

We identified a mechanism for a self-assembling OM machine that can do work. The OM machine converts the incident SAM of the optical beam into outgoing OAM through the CSR of optically assembled NP arrays in an optical trap. Analysis of the scattered light reveals that the CSR is composed of a multitude of collective scattering modes, but only a few modes are significant in terms of outgoing angular momentum, specifically the $e_{7,7}$, $e_{5,-5}$, and $m_{6,-5}$ modes. This OM gear is part of an OM machine that

can transfer the angular momentum scattered in the transverse direction by its collective modes. The scattered light couples to an adjacent probe particle causing the latter to be driven. The resultant OM machine utilizes SAM–OAM conversion similar to that of a planetary gear mechanical machine.

The OM machine operates on two principles. First, the sixfold rotational symmetry of the OM gear allows it to convert the $m_{inc} = 1$ SAM of incident light into $m = 7$ OAM scattered into the transverse plane. This generates a counterclockwise angular driving force on the probe particle, at the expense of a clockwise (negative torque) rotation of the OM gear, consistent with angular momentum conservation. Second, the optical binding interactions of the OM gear give rise to a path for the probe particle's orbital motion with six stable positions. The probe is transported in the counterclockwise direction: Brownian forces activate the particle out of a stable location while the asymmetric force field from the OM gear creates a bias, reminiscent of the concept of a Brownian ratchet [42,43].

In principle, larger OM machines can be designed by increasing the size of the gear (more particles) or by combining multiple smaller gears. It was sufficient to consider $q \in [-1, 0, 1]$ in Eq. (2) for the 7NP structure studied here, but larger gears can access larger outgoing m. With the sixfold symmetry of hexagonal ordering, modes such as $e_{13,13}$ can be accessed, which can create greater OAM and a flatter angular profile than the $e_{7,7}$ mode considered here. OM machines composed of high-index dielectric particles—which have received attention in the plasmonic community for their tunable Mie resonances [44]—are also possible to realize. A silicon OM machine is realized in simulation, and offers several potential advantages over the plasmonic OM machine considered here (see Fig. S12 in Supplement 1). The self-assembling OM machines presented here provide a new and flexible way of controlling and driving matter at the nano-scale, including applications in nanofluidics and particle sorting [45].

APPENDIX A: METHODS

1. Simulation

Electrodynamic simulations were performed with the generalized multiparticle Mie theory (GMMT) using our developed software, MiePy [46]. 150 nm Ag NPs were used to construct the OM gear, while a 200 nm Ag NP was used for the probe particle. The NPs were illuminated with a defocused, converging RHC polarized Gaussian beam with a $1/e^2$ width $w_0 = 2350$ nm, power $P = 40$ mW, and defocus $z = z_R/1.2$, where $z_R = \frac{1}{2}kw_0^2$ is the Rayleigh range and $k = 2\pi n_b/\lambda$. Figure S1 compares the simulated optical setup to the experiment optical setup. A multipole decomposition method we developed was used to identify the scattered modes from the OM gear (see Supplement 1). For the Brownian dynamics simulation, forces on particles were computed by analytic expressions for the integrated Maxwell stress tensor. These electrodynamic forces were used in an over-damped Langevin equation to integrate the equation of motion for the OM gear–probe system (1 μs time step). A trajectory of the simulated OM machine is shown in Visualization 1. See Supplement 1 for further simulation details.

2. Experiment

Experiments were conducted using a single-beam circularly polarized optical tweezer in an inverted microscope setup as described in [20]. A dilute water solution with a mixture of PVP-coated 150 nm Ag NPs and 180–200 nm NPs was used. A cw Ti-sapphire laser beam ($\lambda = 800$ nm) was focused near the glass coverslip using a $60\times$ microscope objective, pushing a small number of NPs toward the glass surface. The laser power was 200 mW before entering the microscope, where additional power is lost in the objective (Nikon $60\times$ SAPO) before focusing toward the sample. A spatial light modulator (SLM; Meadowlark) was used to slightly defocus the trapping beam such that it was converging at the sample. Electrostatic repulsion between the ligands on the NPs and the glass coverslip balances the radiation pressure, resulting in a 2D trapping environment. Trajectories of the experimentally observed OM machines are shown in Visualization 2 and Visualization 3 for the NP8 and NP7 gears, respectively. Additional experimental details have been published elsewhere [7–9,20].

Disclosures. The authors declare no conflicts of interest.

See Supplement 1 for supporting content.

REFERENCES

1. A. Ashkin, J. M. Dziedzic, J. Bjorkholm, and S. Chu, "Observation of a single-beam gradient force optical trap for dielectric particles," Opt. Lett. **11**, 288–290 (1986).
2. R. W. Bowman and M. J. Padgett, "Optical trapping and binding," Rep. Prog. Phys. **76**, 026401 (2013).
3. M. M. Burns, J. M. Fournier, and J. A. Golovchenko, "Optical binding," Phys. Rev. Lett. **63**, 1233–1236 (1989).
4. M. M. Burns, J.-M. Fournier, and J. A. Golovchenko, "Optical matter: crystallization and binding in intense optical fields," Science **249**, 749–754 (1990).
5. S. A. Tatarkova, A. E. Carruthers, and K. Dholakia, "One-dimensional optically bound arrays of microscopic particles," Phys. Rev. Lett. **89**, 283901 (2002).
6. V. Demergis and E.-L. Florin, "Ultrastrong optical binding of metallic nanoparticles," Nano Lett. **12**, 5756–5760 (2012).
7. Z. Yan, R. A. Shah, G. Chado, S. K. Gray, M. Pelton, and N. F. Scherer, "Guiding spatial arrangements of silver nanoparticles by optical binding interactions in shaped light fields," ACS Nano **7**, 1790–1802 (2013).
8. Z. Yan, S. K. Gray, and N. F. Scherer, "Potential energy surfaces and reaction pathways for light-mediated self-organization of metal nanoparticle clusters," Nat. Commun. **5**, 3751 (2014).
9. Z. Yan, M. Sajjan, and N. F. Scherer, "Fabrication of a material assembly of silver nanoparticles using the phase gradients of optical tweezers," Phys. Rev. Lett. **114**, 143901 (2015).
10. J. Ng, Z. Lin, C. Chan, and P. Sheng, "Photonic clusters formed by dielectric microspheres: numerical simulations," Phys. Rev. B **72**, 085130 (2005).
11. J. Taylor and G. Love, "Spontaneous symmetry breaking and circulation by optically bound microparticle chains in Gaussian beam traps," Phys. Rev. A **80**, 053808 (2009).
12. S. Albaladejo, J. J. Sáenz, and M. I. Marqués, "Plasmonic nanoparticle chain in a light field: a resonant optical sail," Nano Lett. **11**, 4597–4600 (2011).
13. L. Chvátal, O. Brzobohatý, and P. Zemánek, "Binding of a pair of au nanoparticles in a wide Gaussian standing wave," Opt. Rev. **22**, 157–161 (2015).
14. S. Sukhov, A. Shalin, D. Haefner, and A. Dogariu, "Actio et reactio in optical binding," Opt. Express **23**, 247–252 (2015).
15. V. Karásek, M. Šiler, O. Brzobohatý, and P. Zemánek, "Dynamics of an optically bound structure made of particles of unequal sizes," Opt. Lett. **42**, 1436–1439 (2017).
16. S. H. Simpson, P. Zemánek, O. M. Maragò, P. H. Jones, and S. Hanna, "Optical binding of nanowires," Nano Lett. **17**, 3485–3492 (2017).
17. F. Nan, F. Han, N. F. Scherer, and Z. Yan, "Dissipative self-assembly of anisotropic nanoparticle chains with combined electrodynamic and electrostatic interactions," Adv. Mater. **30**, 1803238 (2018).
18. Y. Yifat, D. Coursault, C. W. Peterson, J. Parker, Y. Bao, S. K. Gray, S. A. Rice, and N. F. Scherer, "Reactive optical matter: light-induced motility in electrodynamically asymmetric nanoscale scatterers," Light Sci. Appl. **7**, 105 (2018).
19. J. Chen, J. Ng, K. Ding, K. H. Fung, Z. Lin, and C. T. Chan, "Negative optical torque," Sci. Rep. **4**, 6386 (2014).
20. F. Han, J. A. Parker, Y. Yifat, C. Peterson, S. K. Gray, N. F. Scherer, and Z. Yan, "Crossover from positive to negative optical torque in mesoscale optical matter," Nat. Commun. **9**, 4897 (2018).
21. J. Chen, S. Wang, X. Li, and J. Ng, "Mechanical effect of photonic spin-orbit interaction for a metallic nanohelix," Opt. Express **26**, 27694–27704 (2018).
22. S. Sukhov and A. Dogariu, "Non-conservative optical forces," Rep. Prog. Phys. **80**, 112001 (2017).
23. Y. Roichman and D. G. Grier, "Three-dimensional holographic ring traps," Proc. SPIE **6483**, 64830F (2007).
24. J. Damková, L. Chvátal, J. Ježek, J. Oulehla, O. Brzobohatý, and P. Zemánek, "Enhancement of the 'tractor-beam' pulling force on an optically bound structure," Light Sci. Appl. **7**, 17135 (2018).
25. C. W. Peterson, J. Parker, S. A. Rice, and N. F. Scherer, "Controlling the dynamics and optical binding of nanoparticle homodimers with transverse phase gradients," Nano Lett. **19**, 897–903 (2019).
26. F. G. De Abajo, "Colloquium: light scattering by particle and hole arrays," Rev. Mod. Phys. **79**, 1267–1290 (2007).
27. A. La Porta and M. D. Wang, "Optical torque wrench: angular trapping, rotation, and torque detection of quartz microparticles," Phys. Rev. Lett. **92**, 190801 (2004).
28. F. Pedaci, Z. Huang, M. Van Oene, S. Barland, and N. H. Dekker, "Excitable particles in an optical torque wrench," Nat. Phys. **7**, 259–264 (2011).
29. J. Inman, S. Forth, and M. D. Wang, "Passive torque wrench and angular position detection using a single-beam optical trap," Opt. Lett. **35**, 2949–2951 (2010).
30. L. Tong, V. D. Miljkovic, and M. Kall, "Alignment, rotation, and spinning of single plasmonic nanoparticles and nanowires using polarization dependent optical forces," Nano Lett. **10**, 268–273 (2010).
31. Z. Yan and N. F. Scherer, "Optical vortex induced rotation of silver nanowires," J. Phys. Chem. Lett. **4**, 2937–2942 (2013).
32. N. Sule, Y. Yifat, S. K. Gray, and N. F. Scherer, "Rotation and negative torque in electrodynamically bound nanoparticle dimers," Nano Lett. **17**, 6548–6556 (2017).
33. V. Blickle and C. Bechinger, "Realization of a micrometre-sized stochastic heat engine," Nat. Phys. **8**, 143–146 (2012).
34. A. Dechant, N. Kiesel, and E. Lutz, "All-optical nanomechanical heat engine," Phys. Rev. Lett. **114**, 183602 (2015).
35. I. A. Martínez, É. Roldán, L. Dinis, D. Petrov, J. M. Parrondo, and R. A. Rica, "Brownian Carnot engine," Nat. Phys. **12**, 67–70 (2016).

36. A. Canós Valero, D. Kislov, E. A. Gurvitz, H. K. Shamkhi, A. A. Pavlov, D. Redka, S. Yankin, P. Zemánek, and A. S. Shalin, "Nanovortex-driven all-dielectric optical diffusion boosting and sorting concept for lab-on-a-chip platforms," Adv. Sci. **7**, 1903049 (2020).

37. J. J. Coy, D. P. Townsend, and E. V. Zaretsky, "Gearing," Technical Report 84-C-15 (National Aeronautics and Space Administration Cleveland Oh Lewis Research Center, 1985).

38. A. R. Edmonds, *Angular Momentum in Quantum Mechanics* (Princeton University, 1996), Vol. **4**.

39. T. A. Nieminen, T. Asavei, V. L. Loke, N. R. Heckenberg, and H. Rubinsztein-Dunlop, "Symmetry and the generation and measurement of optical torque," J. Quant. Spectrosc. Radiat. Transfer **110**, 1472–1482 (2009).

40. W. J. Wiscombe, "Improved Mie scattering algorithms," Appl. Opt. **19**, 1505–1509 (1980).

41. S. Zou, N. Janel, and G. C. Schatz, "Silver nanoparticle array structures that produce remarkably narrow plasmon lineshapes," J. Chem. Phys. **120**, 10871–10875 (2004).

42. H. Risken and H. Vollmer, "Brownian motion in periodic potentials; nonlinear response to an external force," Z. Phys. B **33**, 297–305 (1979).

43. M. O. Magnasco, "Forced thermal ratchets," Phys. Rev. Lett. **71**, 1477–1481 (1993).

44. A. I. Kuznetsov, A. E. Miroshnichenko, M. L. Brongersma, Y. S. Kivshar, and B. Luk'yanchuk, "Optically resonant dielectric nanostructures," Science **354**, aag2472 (2016).

45. F. Nan and Z. Yan, "Sorting metal nanoparticles with dynamic and tunable optical driven forces," Nano Lett. **18**, 4500–4505 (2018).

46. https://github.com/johnaparker/miepy.